Complete quantification of parametric uncertainties in (d,p) transfer reactions

M. Catacora-Rios,[1,2] A. E. Lovell,[3] and F. M. Nunes[1,2]

[1]*Department of Physics and Astronomy, Michigan State University, East Lansing, Michigan 48824-1321, USA*
[2]*Facility for Rare Isotope Beams, Michigan State University, East Lansing, Michigan 48824, USA*
[3]*Theoretical Division, Los Alamos National Laboratory, Los Alamos, New Mexico 87545, USA*

(Received 3 January 2023; revised 9 June 2023; accepted 12 July 2023; published 2 August 2023)

Background: Deuteron-induced transfer reactions are a popular probe in nuclear structure and nuclear astrophysics studies. The interpretation of these transfer measurements relies on reaction theory that takes as input effective interactions between the nucleons and the target nucleus.
Purpose: Previous work quantified the uncertainty associated with the optical potentials between the nucleons and the target. In this study, we extend that work by also including the parameters of the mean field associated with the overlap function of the final bound state, thus obtaining the full parametric uncertainty on transfer observables.
Method: We use Bayesian Markov chain Monte Carlo simulations to obtain parameter posterior distributions. We use elastic-scattering cross sections to constrain the optical potential parameters and use the asymptotic normalization coefficient of the final state to constrain the bound-state interaction. We then propagate these posteriors to the transfer angular distributions and obtain confidence intervals for this observable.
Results: We study (d,p) reactions on ^{14}C, ^{16}O, and ^{48}Ca at energies in the range $E_d = 7-24$ MeV. Our results show a strong reduction in uncertainty by using the asymptotic normalization coefficient as a constraint, particularly, for those reactions most sensitive to ambiguities in the mean field. For those reactions, the importance of constraining the bound-state interaction is equal to that of constraining the optical potentials. The case of ^{14}C is an outlier because the cross section is less sensitive to the nuclear interior.
Conclusions: When minimal constraints are used on the parameters of the nucleon-target interaction, the 1σ uncertainties on the differential cross sections are large (≈50–100%). However, if elastic-scattering data and the asymptotic normalization coefficient are used in the analysis, with an error of 10% (5%), this uncertainty reduces to ≈30% (≈15%).

DOI: 10.1103/PhysRevC.108.024601

I. INTRODUCTION

For decades, transfer reactions have been successfully used as a probe in nuclear structure and nuclear astrophysics [1,2]. While many of these studies have focused on investigating single-particle states in nuclei (e.g., Refs. [3,4]), recent efforts [5,6] have also explored transfer as a probe for significantly deformed nuclei. In either case, the interpretation of the results relies on a reaction model.

Theoretical advances for transfer reactions have focused primarily on deuteron-induced reactions [e.g., $A(d,p)B$, $A(d,n)C$]. While there are experiments that still use the distorted-wave Born approximation in the analysis (a perturbative method that, in its standard first-order implementation, simplifies the deuteron incoming wave to the elastic channel [7]), nowadays most studies include deuteron breakup nonperturbatively in the reaction mechanism because it is known to be important. Amongst these nonperturbative methods is the adiabatic distorted-wave approximation (ADWA) [8]. The ADWA treats the excitation energy of the deuteron adiabatically and captures the three-body dynamics in the region where it is necessary. In the ADWA, the inputs are the pairwise interactions: The nucleon-target optical potentials (U_{nA} and U_{pA}) and the effective interactions describing the two relevant bound states (the deuteron V_{np} and the final state V_{nA}). These input interactions are not well known and introduce large uncertainties.

The need for uncertainty quantification in reactions has been identified as an important priority in the community [9]. To extract meaningful information from transfer reactions, be it orbital occupancies or capture rates for astrophysics, it is crucial to know the theoretical uncertainties. Over the last few years, significant effort has been devoted to quantifying uncertainties on the nucleon optical potential when using elastic scattering as a constraint [10–17]. The Bayesian approach first explored in the context of nuclear reactions by Lovell and Nunes [12] offers a rich set of statistical tools to explore the parameter space and provide diagnostics for reducing uncertainties. Within the Bayesian analysis, propagation of optical model uncertainties to (d,p) transfer observables is straightforward (e.g., Refs. [12,14,15]). However, so far, the uncertainties coming from the bound-state descriptions have not been quantified.

While the deuteron bound state is comparatively well known, usually the final state being populated through (d,p) or (d,n) is not. Earlier studies have pointed out the large

ambiguity associated with the choice of parameters for the mean field in the final state [18,19]. As a consequence, the combined method was suggested as a way to reduce this ambiguity: The analysis of transfer (d,p) should be combined with an independent peripheral measurement from which the asymptotic normalization of the final state (the so-called asymptotic normalization coefficient, ANC) can be extracted. Amongst the various peripheral reactions that can be used to extract ANCs are Coulomb dissociation and direct neutron capture reactions (e.g., Refs. [20]), in addition to sub-Coulomb transfer reactions [19,21]. Using the constraint on the ANC in the analysis of the nonperipheral transfer reaction provides a better handle on the abovementioned ambiguities. However, it should be noted that none of these earlier works [18,19] contain a statistical analysis of uncertainties.

In this work, we perform a Bayesian analysis of (d,p) transfer reactions taking into account both the parametric uncertainties associated with the optical potentials and the mean field describing the final bound state. We constrain the bound state with an independent extraction of the ANC, and we constrain the optical potential with elastic scattering, as done before. We then discuss the relative impact of these two sources of uncertainty in the resulting transfer cross sections. To span a variety of cases, we consider one-neutron transfer reactions on ^{14}C, ^{16}O, and ^{48}Ca at energies in the range $E_d = 7-24$ MeV for which real data exist (e.g., Refs. [22–28]). In Sec. II, we briefly present the theoretical framework used, and in Sec. III, we introduce the numerical details of the calculations. Results are presented and discussed in Sec. IV, and the conclusions are drawn in Sec. V.

II. THEORETICAL FRAMEWORK

A. Statistical considerations

1. Bayesian methods

Unlike frequentist methods, Bayesian statistics give the probability of a single occurrence given a model and some prior information. This provides a robust methodology to study uncertainty propagation, model comparison, and model mixing. Bayes' theorem states that for some hypothesis H, model M, and experimental data D [29],

$$p(H|D,M) = \frac{p(D|H,M)p(H|M)}{p(D|M)}. \tag{1}$$

That is, the posterior probability $p(H|D,M)$ of a hypothesis given some data and model is equal to the prior distribution $p(H|M)$ (containing information known about the model before looking at the data) times the likelihood $p(D|H,M)$ (containing information of the goodness of the fit between the hypothesis of the model and the data, which for our application is defined in Ref. [12]). The Bayes' factor $p(D|M)$ in the denominator is the sum of all possible hypotheses of the model space allowed by the prior information and weighted by the likelihood. In previous studies, Bayesian methods have been used to compare uncertainties coming from different data sets and observables [15,16], including the use of the Bayes' factor [17].

In the work presented here, we are concerned with quantifying the uncertainties of transfer reactions using few-body methods. We perform this analysis in a two-step process. First, we use the Bayesian prescription to optimize independently the parameters of our model using several elastic-scattering and ANC data sets. This allows us to quantify the uncertainties in the nucleon-target optical potentials describing the interactions of our model (Secs. II A 2 and II B 1). Second, we propagate the quantified uncertainties from the optimization procedure to the different parts of the few-body transfer matrix using the ADWA (Sec. II B 2).

2. Optical model optimization

In this work, we use the optical model to describe the effective interactions of the nucleon-target scattering states. Optical potentials contain real and imaginary parts describing the elastic channel and absorption into nonelastic channels. The nuclear part of the optical potential typically contains three parts: A volume term, a surface term, and a spin-orbit term, all of Woods-Saxon shape or derivative of Woods-Saxon shape, each term parametrized by a depth, a radius, and a diffuseness:

$$\begin{aligned} U(R) = &-V_o f_{\rm WS}(R;r_o,a_o) - iW_v f_{\rm WS}(R;r_w,a_w) \\ &- i4a_s W_s \frac{d}{dR} f_{\rm WS}(R;r_s,a_s) \\ &+ V_{\rm SO}\frac{1}{R}\frac{d}{dR} f_{\rm WS}(R;r_{\rm so},a_{\rm so}) + V_{\rm C}(R,r_c), \end{aligned} \tag{2}$$

where $f_{\rm WS}(R;r_i,a_i) = \frac{1}{1+\exp[(r-r_i)/a_i]}$, $V_{\rm SO}$ contains the $(\vec{L}\cdot\vec{S})$ term, and $V_{\rm C}$ is the point-sphere Coulomb interaction. The optimization using Bayesian methods is performed on the parameters of the volume and surface terms [first three terms in Eq. (2)], while the parameters of the spin-orbit and Coulomb terms are kept fixed [7].

B. Reaction theory

As mentioned in the previous subsection, we are interested in transfer reactions. In particular, we look at one-neutron transfer reactions of the form $A(d,p)B$(g.s.), where the final state of $B = A + n$ is in the ground state and is described as a single-particle state. The low binding energy of the deuteron allows us to describe (d,p) reactions using the three-body Hamiltonian of the system $n + p + A$:

$$\mathcal{H}_{\rm 3B} = T_R + T_r + U_{nA} + U_{pA} + V_{np}, \tag{3}$$

where U_{pA} and U_{nA} are the effective interactions of the nucleon-target systems and V_{np} is the nucleon-nucleon interaction. T_R and T_r denote the two-body kinetic operators for the deuteron-target and n-p systems, respectively, where r is the relative distance in the n-p system and R is the distance between the center of mass of the n-p system and the target. In the three-body post form [7], we can write the T matrix as

$$T^{\rm exact} = \langle \phi_{I_A I_B} \chi^{(-)}_{pB} | V_{np} + U_{nA} - U_{pB} | \Psi^{\rm exact} \rangle. \tag{4}$$

Here, $\Psi^{\rm exact}$ is the full solution of the three-body $A + n + p$ problem in the incident channel, $\phi_{I_A I_B}$ is the overlap of the

$B = A + n$ and A bound-state wave functions, and $\chi_{pB}^{(-)}$ is the proton distorted wave of the exit channel.

1. Asymptotic normalization coefficient

A central element of the analysis of the $A(d,p)B$(g.s.) reaction, not included in previous uncertainty propagation analyses, is the many-body radial overlap function $\phi_{I_A I_B}$, which depends on the vector-radius ρ connecting the center of mass of A and n. The wave function for the $B = A + n$ system is a bound state, and so it behaves as a spherical Hankel function in the exterior region ($\rho \to \infty$) where the nuclear potential is negligible,

$$\phi_{I_A I_B (l\,j)}(\rho) \overset{\rho\to\infty}{\approx} i\kappa C_{l\,j} h_l(i\kappa\rho). \tag{5}$$

In the above equation, we have $\kappa = \sqrt{2\mu_{An}\epsilon_{An}}$, where μ_{An} and ϵ_{An} are the reduced mass and the binding energy of the $A + n$ system. We also introduce the quantum numbers l and j for $A - n$ relative orbital and total angular momentum. Finally, $C_{l\,j}$ is the ANC. Assuming that the many-body overlap function is proportional to the single-particle function, the experimental ANC, C, and the spectroscopic factor, S, can be related via the following equation:

$$C_{lj}^2 = S_{n_\rho l j} b_{n_\rho l j}^2. \tag{6}$$

Note that here we used the asymptotic properties of the single-particle wave function:

$$u_{n_\rho,l,j}^{nA}(\rho) \overset{\rho\to\infty}{\approx} i\kappa b_{n_\rho l j} h_l(i\kappa\rho), \tag{7}$$

where the single-particle wave function $u_{n_\rho,l,j}^{nA}$ is generated by adjusting a Woods-Saxon-shaped potential with parameters V_o, r_o, and a_o to reproduce the correct separation energy of the bound state with the correct quantum numbers (n_ρ, l, j). Here n_ρ is the principal quantum number. We have introduced the asymptotic normalization coefficient of $u_{n_\rho,l,j}^{nA}$ as $b_{n_\rho l j}$. The relationship in Eq. (6) demonstrates that the ANC is directly related to the spectroscopic factor and, therefore, can be used to reduce the uncertainties in (d,p) reactions.

2. ADWA

The expression for the T matrix in Eq. (4) can be further simplified, as shown by Johnson and Tandy, due to the fact that the exact three-body wave function Ψ^{exact} is only required within the small range of the potential V_{np} [8]. One can then use the Weinberg basis to expand the exact three-body wave function. Neglecting the excitation of the n-p system in the reaction and using only the first term in the expansion, one obtains the adiabatic form of the T matrix:

$$T = \langle u_{nA}\chi_{pB}^{(-)} | V_{np} | \phi_{np}\chi_d^{\text{ad}} \rangle, \tag{8}$$

where we have dropped the remnant term in the operator $U_{nA} - U_{pB}$. We also note that, in the above, we have replaced the many-body overlap function by the single-particle bound state. The adiabatic function χ_d^{ad} is generated from the effective adiabatic potential

$$U_{Ap}^{\text{eff}} = -\langle \phi_o(r) | V_{np}(U_{nA} + U_{pA}) | \phi_o(r) \rangle, \tag{9}$$

where ϕ_o is the first Weinberg state. This method is referred to as the ADWA (see Ref. [8] for a detailed discussion).

TABLE I. Quantum numbers, neutron separation energies, and experimental ANCs squared for the cases considered in this Bayesian analysis.

Bound state	s	l	j	B.E. (MeV)	C_{exp}^2 (fm^{-1})
^{15}C(g.s.)	0.5	0	0.5	1.280	1.48
^{17}O(g.s.)	0.5	2.0	2.5	4.143	0.67
^{49}Ca(g.s.)	0.5	1.0	1.5	5.146	32.1

In this study we only consider local V_{nA} interactions (see Ref. [30] for work on incorporating nonlocal interactions into the framework). Eventually, when comparing to transfer data, one multiplies the right-hand side of Eq. (8) by the spectroscopic factor S.

As in previous work (e.g., Refs. [15–17]), we use elastic-scattering data and our Bayesian procedure to constrain the entrance channel effective potentials of the nucleon-target system in Eq. (9). The same procedure also constrains the proton distorted wave of the exit channel $\chi_{pB}^{(-)}$ in Eq. (8). By now including the ANC in the analysis, we can put a parametric constraint on the last piece of the puzzle, the overlap function of the bound state, u_{An}. In this way, we obtain a full parametric uncertainty analysis of (d,p) transfer reactions using Bayesian statistics.

III. METHODS AND NUMERICAL DETAILS

In our Bayesian analysis, we aim to fit a theoretical model prediction, $\sigma^{\text{th}}(\mathbf{x})$ (corresponding to some set of parameters $\mathbf{x}$), to a set of experimental data, σ_i^{exp}, with some experimental error ε_i. The corresponding set of parameters $\mathbf{x}$ for each nucleon-target interaction is optimized separately using data for each reaction. Two types of reaction data are used in this paper, the ANC and differential elastic-scattering cross sections.

A. ANC fitting

The first type of data, σ_i^{exp}, considered here is the ANCs extracted from previous work (references provided in Table II). These ANCs are used to constrain the single-particle bound-state wave function in the T matrix of Eq. (8). For this type of data, our theoretical model σ^{th} consists of the single-particle potential for $B = A + n$ described by a real volume term and a spin-orbit term. Our Bayesian analysis of the ANC only samples the real radius r_o and the real diffuseness a_o of the volume term. For each two-dimensional parameter draw $\mathbf{x} = (r_o, a_0)$, the real volume depth V_o is adjusted to reproduce the correct neutron separation energy of the system. The spin-orbit term, although included in the model, remains fixed and is, thus, not part of the Bayesian analysis. The quantum numbers, neutron separation energies, and experimental C^2's are summarized in Table I.

B. Elastic fitting

The second type of data σ_i^{exp} used in this work is the elastic-scattering angular distributions $(d\sigma/d\Omega)$ that constrain the nucleon-target interactions for the incoming and outgoing channels. As in our previous work (see Refs. [12,16]

TABLE II. Data type (column 4) and number of parameters being optimized independently (column 3) for each of the reactions or bound states (column 1) at the given reaction energy or neutron binding energy (column 2) considered in the Bayesian analysis.

Reaction/bound state	Energy (MeV)	dim(**x**)	Data type
^{15}C(g.s.)	−1.280	2	$C^2_{\rm exp}$ [32]
^{14}C$(p,p)^{14}$C	8.5	9	$(d\sigma/d\Omega)_{\rm mock}$
^{14}C$(n,n)^{14}$C	8.5	9	$(d\sigma/d\Omega)_{\rm mock}$
^{14}C$(p,p)^{14}$C	17	9	$(d\sigma/d\Omega)_{\rm mock}$
^{17}O(g.s.)	−4.143	2	$C^2_{\rm exp}$ [33]
^{16}O$(p,p)^{16}$O	7.5	9	$(d\sigma/d\Omega)_{\rm mock}$
^{16}O$(n,n)^{16}$O	7.5	9	$(d\sigma/d\Omega)_{\rm mock}$
^{16}O$(p,p)^{16}$O	15	9	$(d\sigma/d\Omega)_{\rm mock}$
^{49}Ca(g.s.)	−5.146	2	$C^2_{\rm exp}$ [19]
^{48}Ca$(p,p)^{48}$Ca	12	9	$(d\sigma/d\Omega)_{\rm mock}$
^{48}Ca$(n,n)^{48}$Ca	12	9	$(d\sigma/d\Omega)_{\rm mock}$
^{48}Ca$(p,p)^{48}$Ca	24	9	$(d\sigma/d\Omega)_{\rm mock}$

for details), our optical model $\sigma^{\rm th}$ now consists of real and imaginary volume terms, a surface term, a spin-orbit term, and a Coulomb term as in Eq. (3). We use elastic mock data as was done in Refs. [15–17]. The mock data are generated from the Koning-Delaroche (KD) optical model [31]. To fit the mock data, we optimize parameter sets consisting of the real and imaginary volume terms and the surface term, for a total of nine parameters, $\mathbf{x} = (V_o, r_o, a_o, W_v, r_w, a_w, W_s, r_s, a_s)$. The spin-orbit and Coulomb terms are kept fixed to the KD value used to generate the mock data. Table II summarizes the number of parameters being fitted for each reaction (dim, column three) and the type of data used (column four).

C. Numerical details

As in previous work, we use the Metropolis-Hastings Markov chain Monte Carlo (MH-MCMC, see Ref. [12] for numerical details). Our optical potential parameters are initialized with the Becchetti-Greenlees (BG) parametrization [34]. We introduce the following shorthand notation for the percent error in the data, $\varepsilon_5 = 0.05\sigma^{\rm exp}$, $\varepsilon_{10} = 0.1\sigma^{\rm exp}$, and $\varepsilon_{100} = 1.0\sigma^{\rm exp}$, corresponding to 5%, 10%, and 100% error on the data. Our prior distributions are Gaussian and centered around the BG value with a width equal to 20% of the mean distribution. As was done in Ref. [17], if any of the imaginary potential depths is equal to zero, we set it to 1 MeV and give it a width of 10 MeV. Using the MH-MCMC, we draw parameter sets **x** until 16 000 sets are accepted and we keep one of every ten of these. These 1600 pulls constitute our posterior distributions. The computations are performed using the QUILTR code [16,35]. Using the posterior distributions from the bound-state and elastic-scattering sampling, we generate predictions for the ADWA transfer cross section using QUILTR, which embeds the transfer code NLAT [36].

IV. RESULTS

The main goal of this work is to include the parametric uncertainties of the bound state, on top of the uncertainties arising from the optical model, into the analysis of transfer reactions, thus obtaining the full parametric uncertainty quantification for the predicted observables.

A. Constraining the bound state

As a first step, we quantify the parametric uncertainties obtained by constraining only the bound state using the ANC (C^2) and then propagating this uncertainty via the T matrix in Eq. (8). As mentioned in the previous section, the effective interactions for the $A + n$ bound states consist of a real volume term and a spin-orbit term; of these, we sample independently the radius (r_o) and diffuseness (a_o) adjusting the depth (V_o) to reproduce the correct binding energies of the bound state. The means of the prior distributions are chosen to reproduce the experimental ANC. In Fig. 1, we show the accepted parameter correlations (off-diagonal plots), posterior distributions (diagonal histograms), and prior distributions (green line in the diagonal histograms).

We have studied the parameter constraint obtained with the ANC (C^2) when the experimental error on C^2 is changed from 10% (ε_{10}) in brown to 100% (ε_{100}) in teal. In Fig. 1(a), we show the parameters of the ^{15}C bound state; in Fig. 1(b), we show the parameters for the ^{17}O bound state; and in Fig. 1(c), we show the parameters for the ^{49}Ca bound state.

In Table III, the mean value and the standard deviation of the posteriors are given for each bound state and C^2 experimental error (ε_{10} or ε_{100}). As expected, there is an increase in the width of the posteriors when increasing the experimental error since then a larger set of parameter combinations can be accepted into the Bayesian optimization. The tightened constraint on the parameters from a smaller error on C^2 results in a stronger correlation between r_o and a_o (see off-diagonal plots in Fig. 1). One should keep in mind that, because the depth (V_o) is not directly sampled, it is strongly correlated with r_o.

Now, we propagate the uncertainties to the differential transfer cross sections. First, we only allow the bound-state parameters to vary, while all other interactions are held constant, including all optical potentials. The 68% confidence intervals for the predicted transfer cross section are shown in Fig. 2 (left panels): Panel (a) for ^{14}C(d,p) ^{15}C(g.s.), panel (c) for ^{16}O(d,p) ^{17}O(g.s.), and panel (e) for ^{48}Ca(d,p) ^{49}Ca(g.s.). The right panels (b), (d), and (f) provide the corresponding percent error plots, obtained from the width of the 68% confidence interval divided by the mean at every angle ($\Delta\sigma/\bar{\sigma}$). The results using 10% error (100%) on the ANC squared are in brown (teal). We can clearly see that reducing the experimental error from 100% to 10% leads to a large decrease in the uncertainty of the transfer cross section, for all reactions shown.

We first focus on Figs. 2(a) and 2(b). The ^{14}C(d,p) ^{15}C(g.s.) is special in that it populates the halo state in ^{15}C. Because, in the ground state of ^{15}C, the neutron is in a loosely bound s wave, at leading order, the ANC is provided by the one-neutron separation energy and independent of the parameters of the mean field [37]. The corresponding transfer reaction is mostly peripheral and, therefore, not very sensitive to details of the single-particle bound-state

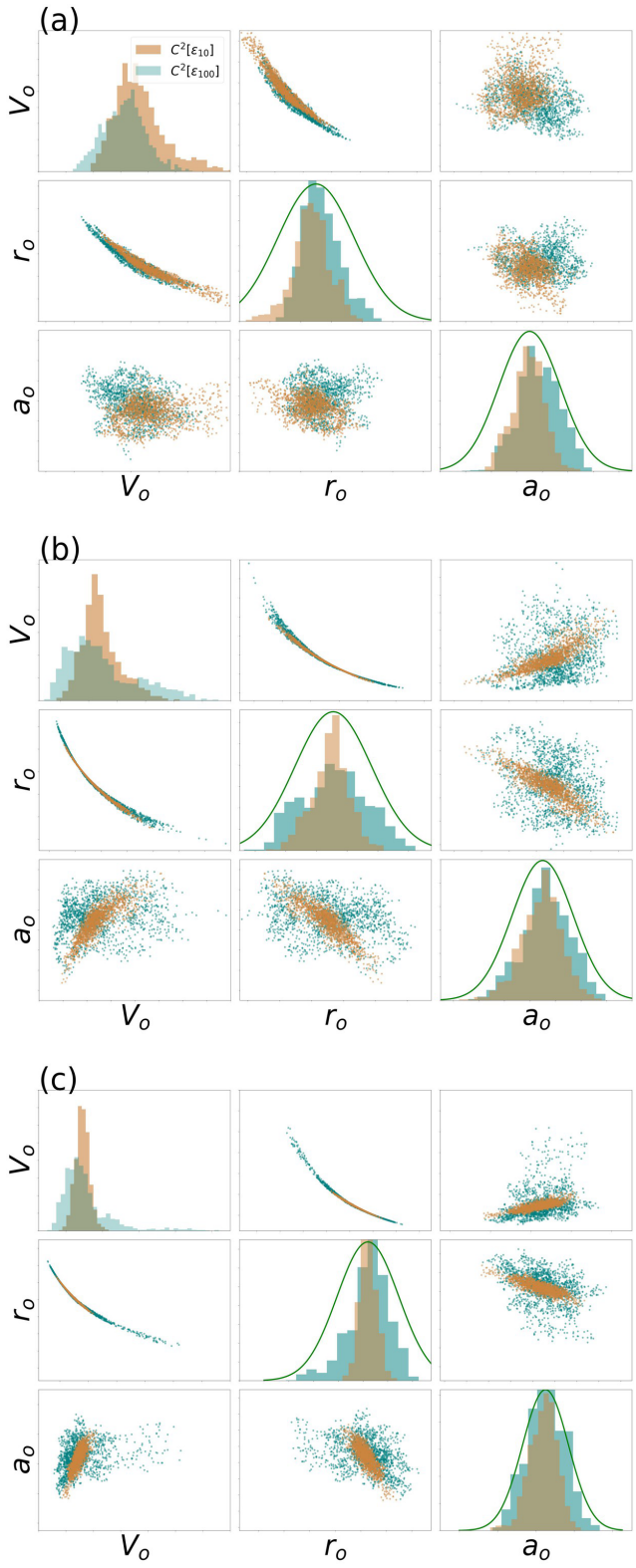

FIG. 1. Parameter posteriors and correlations for single-particle parameters of (a) the ^{15}C bound state, (b) the ^{17}O bound state, and (c) the ^{49}Ca bound state, using Bayesian optimization to compare two different experimental errors on C^2, $\varepsilon_{10}(\varepsilon = 10\%)$ shown in brown and $\varepsilon_{100}(\varepsilon = 100\%)$ shown in teal. Histograms on the diagonal correspond to the posterior distributions of the given parameters; the priors are shown in green.

TABLE III. Posterior means and standard deviations optimized with different experimental errors ε_{C^2} for each bound state studied (column 1), the mean of the real volume term parameters; depth, radius, and diffuseness are listed in the second, third, and fourth columns, respectively (their corresponding standard deviations $\bar{\sigma}$ are in parentheses).

Bound state (ε_{C^2})	$V_o(\bar{\sigma})$ (MeV)	$r_o(\bar{\sigma})$ (fm)	$a_o(\bar{\sigma})$ (fm)
^{15}C (ε_{10})	94.5(19.8)	0.87(0.12)	0.54(0.06)
^{15}C (ε_{100})	82.7(15.2)	0.93(0.15)	0.59(0.08)
^{17}O (ε_{10})	68.7(13.5)	1.09(0.12)	0.64(0.08)
^{17}O (ε_{100})	69.9(24.9)	1.12(0.22)	0.67(0.10)
^{49}Ca (ε_{10})	48.98(3.817)	1.24(0.06)	0.64(0.07)
^{49}Ca (ε_{100})	50.6(13.5)	1.24(0.17)	0.64(0.10)

parameters. As a consequence, even without any constraint on the ANC, the uncertainty from the single-particle bound-state parameters is small. Adding the ANC constraint on the mean-field parameters then offers a modest improvement of less than a factor of 2 at forward angles (modest compared to other cases we study). This does not mean that the ANC should not be used in the analysis, quite the opposite. In the limit of a purely peripheral reaction, the cross section is directly proportional to C^2 and completely insensitive to the single-particle mean-field parameters. In such a case, C^2 is the only quantity of the bound state that matters (apart from the quantum numbers and the binding energy) and the uncertainty coming from the bound state is trivially and uniquely related to the error on C^2. In this work, we are focusing on quantifying the nontrivial uncertainty from the single-particle parameters of the bound state.

The reactions on ^{16}O and ^{48}Ca, representing the more typical cases, are less peripheral. As such, when there is little constraint on the ANC, the uncertainties of the transfer cross section propagating from the single-particle parameters are large (≈60–80). The gain offered by introducing the ANC constraints is a factor of 4 (3) for ^{16}O(^{48}Ca) at forward angles.

For these three targets, we have verified that the uncertainty of the calculated transfer cross section scales with and is directly proportional to the error on the C^2 for sub-Coulomb reactions. In those cases, the uncertainties from the single-particle parameters is negligible.

B. Elastic vs ANC constrain

All results in Sec. IV A assume the optical potentials are fixed. We have studied optical potential uncertainties before (e.g., Refs. [12,14,16,17]); so, next, we proceed by combining the uncertainties from the bound-state interactions with those from the optical potentials, to obtain the full uncertainty quantification (see Table II for a description of the reactions and bound states considered).

Figure 3 contains transfer results for several assumptions. As before, 68% confidence intervals are shown in the left-hand panels and the percentage uncertainties are shown in the right-hand panels, ^{14}C(d,p) ^{15}C(g.s.) [panels (a) and (b)], ^{16}O(d,p) ^{17}O(g.s.) [panels (c) and (d)], and ^{48}Ca(d,p) ^{49}Ca(g.s.) [panels (e) and (f)]. The results in brown

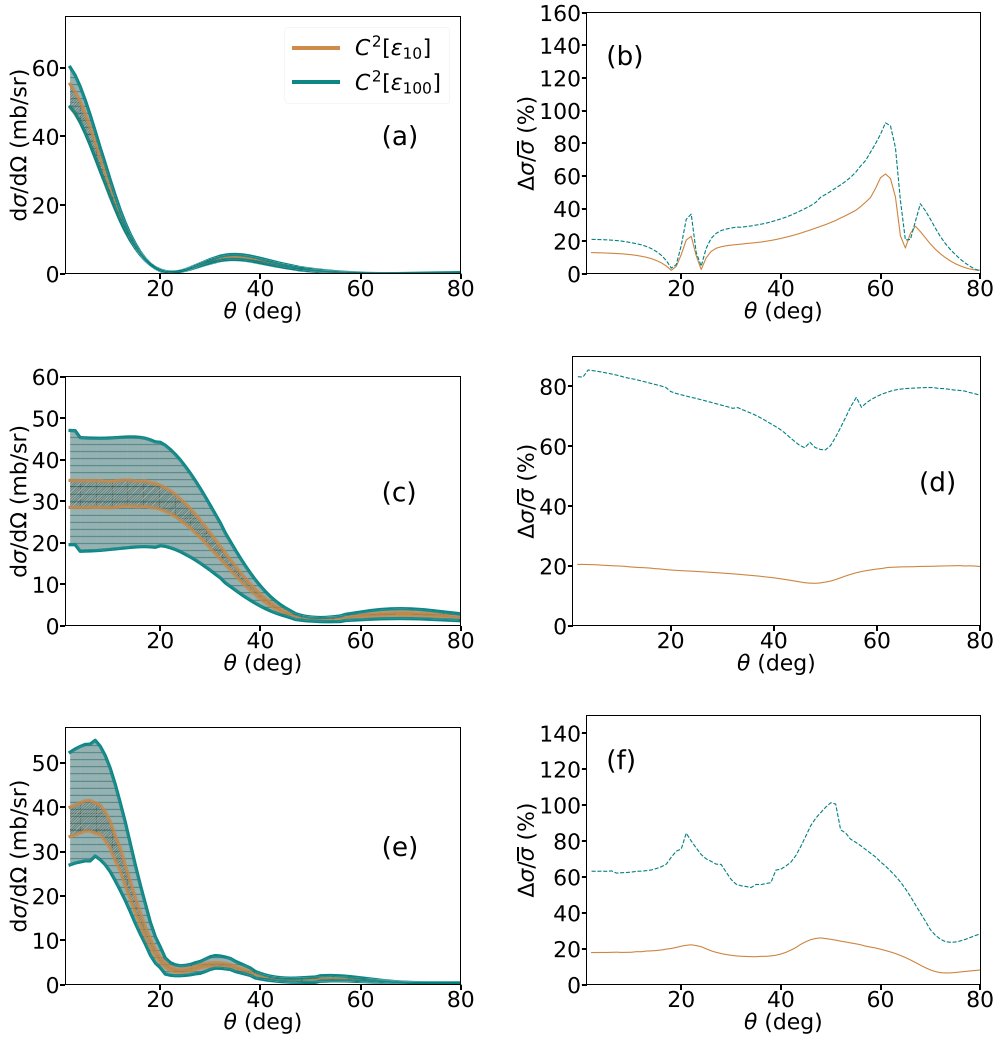

FIG. 2. A comparison of results for transfer assuming two C^2 experimental data errors, 10% error in brown (ε_{10}) and 100% error in teal (ε_{100}). ^{14}C(d,p) at 17-MeV 68% confidence intervals (a) and percentage uncertainty (b). ^{16}O(d,p) at 15-MeV 68% confidence intervals (c) and percentage uncertainty (d). ^{48}Ca(d,p) at 24-MeV 68% confidence intervals (e) and percentage uncertainty (f).

assume no uncertainty on the optical potentials constrained by elastic data (these parameters are fixed to the KD values used to generate the data) and only the uncertainties on the bound-state parameters are constrained through C^2 taking an error of 10% (ε_{10}) just as presented by the brown bands in Fig. 2. The results in bright green are the reverse, we assume no uncertainty on the bound-state interaction and quantify uncertainties only from all optical potentials taking elastic data (el) with 10% uncertainty (ε_{10}). The results in blue incorporate the uncertainties in both the bound-state interaction and the optical potentials assuming the errors on the ANC and elastic-scattering data are 10% ($C^2 + \text{el}$). Finally, the results in gray are the same as those in blue except that the errors are now 100%. Note that the gray band in Fig. 3 does not correspond to the results in teal in Fig. 2. All results in Fig. 2 assume fixed optical potential parameters. The results in gray in Fig. 3 are a lower limit to the "unconstrained" case; they represent only minimal constraint on the parameters of both the bound state and the entrance and exit distorted waves.

From the width of the confidence bands and the percent error plots shown in Fig. 3, we can see that the parametric uncertainties coming from the ANC (C^2) and the elastic (el) constraints are of similar order of magnitude and, therefore, of equal importance. Again we single out the ^{14}C case: Because the uncertainty propagating from the single-particle parameters is small in this case, the optical model uncertainties dominate the problem.

As shown by the wider blue band in Fig. 3, choosing to only propagate the uncertainty of the bound-state interaction or the optical potential parameters can lead to an underrepresentation of the uncertainty in the predicted transfer cross section. Finally, assuming minimal knowledge constraint on the parameters leads to very large errors.

These results are summarized in Table IV, which provides the percent error of the predicted transfer cross section at the first peak of the angular distribution for all cases considered. We choose to quantify the error at this specific angle because the spectroscopic factor (S) is typically extracted around this point: The reaction and the beam energy are given

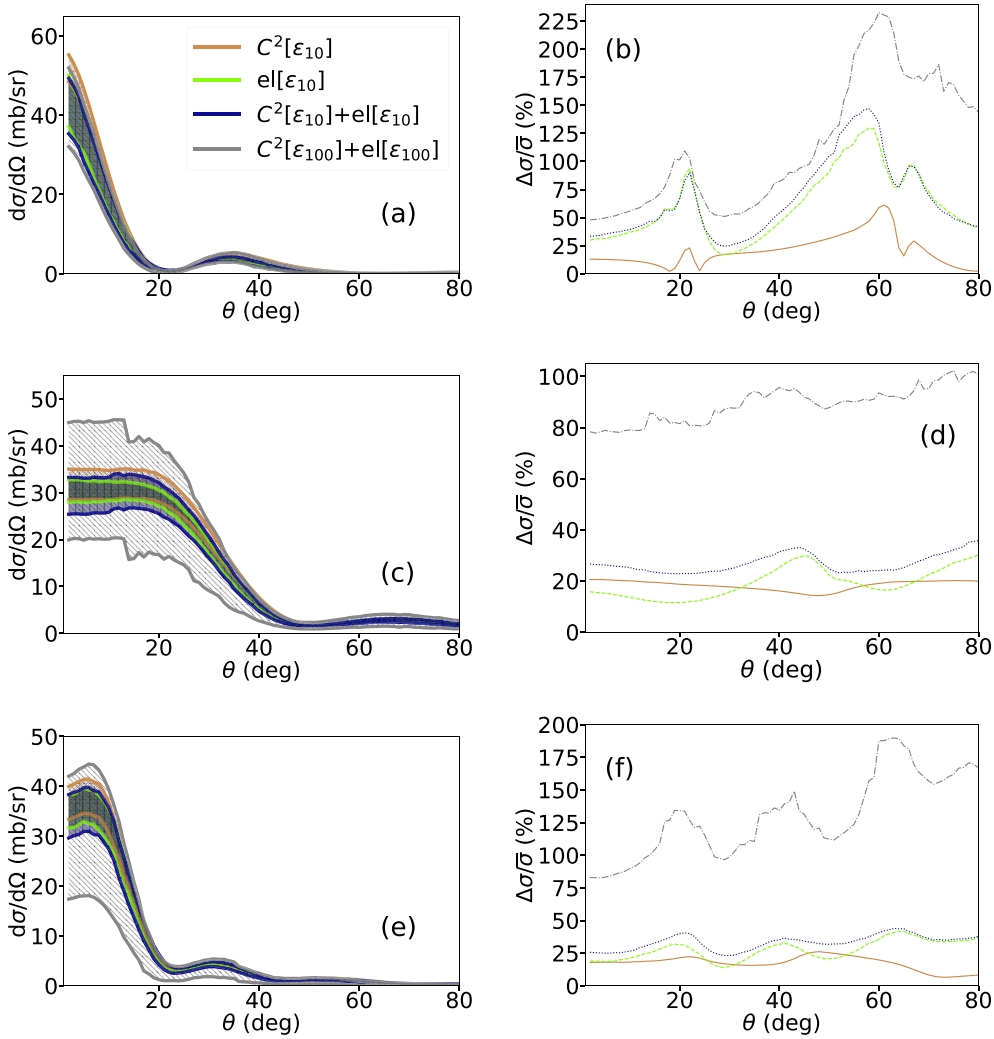

FIG. 3. A comparison of results using only ANC (C^2) data in brown, only elastic data (el) in bright green, and both types of data simultaneously (C^2 + el), all at 10% error (ε_{10}) in blue and unconstrained in gray. (a) and (b) ^{14}C(d,p) at 17-MeV 68% confidence intervals and percentage uncertainty plot. (c) and (d) ^{16}O(d,p) at 15-MeV 68% confidence intervals and percentage uncertainty plot. (e) and (f) ^{48}Ca(d,p) at 24-MeV 68% confidence intervals and percentage uncertainty plot.

in columns 1 and 2, respectively; the data and experimental error used to constrain the parametric uncertainties are provided in column 3; and columns 4 and 5 show the percent error at the peak for 68% and 95% confidence intervals. This analysis shows that, for nonperipheral reactions, constraining the bound-state parameters is equally as important as constraining the nucleon-target interactions determining the incoming and outgoing channels. One might expect that the uncertainties coming from these different interactions would be independent of one another. Our results are consistent with this expectation: The quadrature sum of the error obtained constraining only the bound-state interaction with the ANC and the error obtained constraining only the nucleon-target optical potentials with elastic scattering is equal to the square of the error of constraining both simultaneously, as expected for independent errors.

Constraining only the bound-state parameters or only the optical model parameters provides an inaccurate account of the uncertainties. Note that the brown and bright green bands in Fig. 3, which correspond to constraining either the bound-state interaction only or the optical model parameters only, while fixing the other parameters, are not realistic predictions for uncertainties. These calculations were done to quantify the effects of these two different sources of uncertainty. However, they rely on the unphysical assumption that the fixed parameters are known exactly (with zero error). To assess the uncertainty when no constraint is imposed on the parameters, we take 100% error on both ANC and elastic angular distributions, a way of representing minimal knowledge (shown in gray).

In Fig. 4, we compare the results for the physical situation when only one aspect is constrained, namely, just the bound-state interaction with the ANC (red) or the optical potentials with elastic scattering (green), and the other parameters (so-called unconstrained parameters) have posteriors corresponding to an experimental error of 100%. For comparison, we also include in Fig. 4 the same unconstrained result of Fig. 3 (gray), and the results obtained when both, bound

TABLE IV. Summary of the effect of propagating different combinations of the ANC (C^2) and elastic (el) uncertainties to the peak of the transfer angular distribution. For each reaction and energy considered (columns 1 and 2), and data included in the calculations along with a corresponding error (column 3), the percent error at the peak of the angular distribution of 68% confidence intervals (column 4) and 95% confidence intervals (column 5) are included.

Reaction	E (MeV)	Data [error]	$(\Delta\sigma/\bar{\sigma})^{68}_{\text{peak}}$ (%)	$(\Delta\sigma/\bar{\sigma})^{95}_{\text{peak}}$ (%)
^{14}C$(d,p)^{15}$C(g.s.)	17	$C^2[\varepsilon_{10}]$	13.0	24.7
^{14}C$(d,p)^{15}$C(g.s.)	17	el$[\varepsilon_{10}]$	30.0	63.2
^{14}C$(d,p)^{15}$C(g.s.)	17	$C^2[\varepsilon_5]+$ el$[\varepsilon_5]$	15.4	28.9
^{14}C$(d,p)^{15}$C(g.s.)	17	$C^2[\varepsilon_{10}]+$ el$[\varepsilon_{10}]$	33.3	61.6
^{14}C$(d,p)^{15}$C(g.s.)	17	$C^2[\varepsilon_{10}]+$ el$[\varepsilon_{100}]$	45.8	104.7
^{14}C$(d,p)^{15}$C(g.s.)	17	el$[\varepsilon_{10}]+C^2[\varepsilon_{100}]$	35.5	71.1
^{14}C$(d,p)^{15}$C(g.s.)	17	$C^2[\varepsilon_{100}]+$ el$[\varepsilon_{100}]$	48.1	109.1
^{16}O$(d,p)^{17}$O(g.s.)	15	$C^2[\varepsilon_{10}]$	19.6	44.8
^{16}O$(d,p)^{17}$O(g.s.)	15	el$[\varepsilon_{10}]$	15.5	34.3
^{16}O$(d,p)^{17}$O(g.s.)	15	$C^2[\varepsilon_5]+$ el$[\varepsilon_5]$	12.7	27.1
^{16}O$(d,p)^{17}$O(g.s.)	15	$C^2[\varepsilon_{10}]+$ el$[\varepsilon_{10}]$	24.3	55.6
^{16}O$(d,p)^{17}$O(g.s.)	15	$C^2[\varepsilon_{10}]+$ el$[\varepsilon_{100}]$	33.1	71.7
^{16}O$(d,p)^{17}$O(g.s.)	15	el$[\varepsilon_{10}]+C^2[\varepsilon_{100}]$	78.7	149.3
^{16}O$(d,p)^{17}$O(g.s.)	15	$C^2[\varepsilon_{100}]+$ el$[\varepsilon_{100}]$	78.9	149.9
^{48}Ca$(d,p)^{49}$Ca(g.s.)	24	$C^2[\varepsilon_{10}]$	18.1	34.7
^{48}Ca$(d,p)^{49}$Ca(g.s.)	24	el$[\varepsilon_{10}]$	18.4	36.4
^{48}Ca$(d,p)^{49}$Ca(g.s.)	24	$C^2[\varepsilon_5]+$ el$[\varepsilon_5]$	13.5	25.7
^{48}Ca$(d,p)^{49}$Ca(g.s.)	24	$C^2[\varepsilon_{10}]+$ el$[\varepsilon_{10}]$	24.9	48.7
^{48}Ca$(d,p)^{49}$Ca(g.s.)	24	$C^2[\varepsilon_{10}]+$ el$[\varepsilon_{100}]$	52.4	131.5
^{48}Ca$(d,p)^{49}$Ca(g.s.)	24	el$[\varepsilon_{10}]+C^2[\varepsilon_{100}]$	62.2	135.1
^{48}Ca$(d,p)^{49}$Ca(g.s.)	24	$C^2[\varepsilon_{100}]+$ el$[\varepsilon_{100}]$	84.0	167.4

state and scattering potentials, are constrained with precise data ε_{10} (blue). As before, the 68% confidence intervals for the predicted transfer cross section are shown in the left-hand panels of Fig. 4: (a) ^{14}C$(d,p)^{15}$C(g.s.), (c) ^{16}O$(d,p)^{17}$O(g.s.), and (e) ^{48}Ca$(d,p)^{49}$Ca(g.s.). The corresponding percentage uncertainties as a function of angle are shown in the the right-hand panels of Fig. 4: (b), (d), and (f).

Comparing the blue and gray bands in Fig. 4 gives a good estimate of the incredible improvement obtained when constraining the interactions using quality data. Comparing the green and red bands to the blue band, it is evident that there is only partial gain obtained by just constraining part of the interactions. For all cases, the uncertainties can be brought down to 20–30% if both ANC and elastic-scattering constraints are included. It is also clear, comparing the red and gray lines in Fig. 4(b), that for a peripheral reaction the ANC constraint on the single-particle parameters is not significant, whereas it produces a large reduction of the uncertainty in the forward-angle cross sections for the reactions on ^{16}O and ^{48}Ca [red and gray lines in Figs. 4(d) and 4(f)]. Through calculations not shown here, we determined that the forward-angle cross section for ^{14}C(d,p) at 17 MeV is not sensitive to the wave function at small distances, contrary to the (d,p) reactions on ^{16}O and ^{48}Ca here considered. We find that for the (d,p) reaction populating the halo state in ^{15}C, the parametric uncertainties of the optical potential are much more important than the parametric uncertainties on the single-particle bound state, and as such the elastic scattering offers the best uncertainty reduction.

As before, we can quantify the uncertainties by looking at the percent error at the peak of the transfer angular distribution (shown in Table IV).

C. The effect of the experimental error on parametric uncertainties

Finally, given the rapid advances in beam intensities and detector systems, it is interesting to consider the improvement that can be obtained with high-precision experimental measurements. In this section we show the effects of decreasing the error in the data from 10% to 5%. Figure 5 is similar to Fig. 4: the left-hand panels depict the 68% confidence intervals of the predicted transfer cross sections, (a) ^{14}C$(d,p)^{15}$C(g.s.), (c) ^{16}O$(d,p)^{17}$O(g.s.), and (e) ^{48}Ca$(d,p)^{49}$Ca(g.s.), and the right-hand panels are the corresponding angular percent errors. We plot the results when all of the parameters are constrained by data with 5% errors (magenta) to be compared with the results obtained before, with 10% error (blue). For reference we also include the unconstrained case, corresponding to results obtained when the data have 100% error (gray).

We can observe from the percent errors in Figs. 5(b), 5(d) and 5(f) that the decrease in experimental error unambiguously decreases the uncertainty in the predicted transfer cross sections. This uncertainty is quantified in Table IV. Decreasing the experimental error from 10% to 5% reduces the percent error of the predicted cross section by roughly a factor of 2.

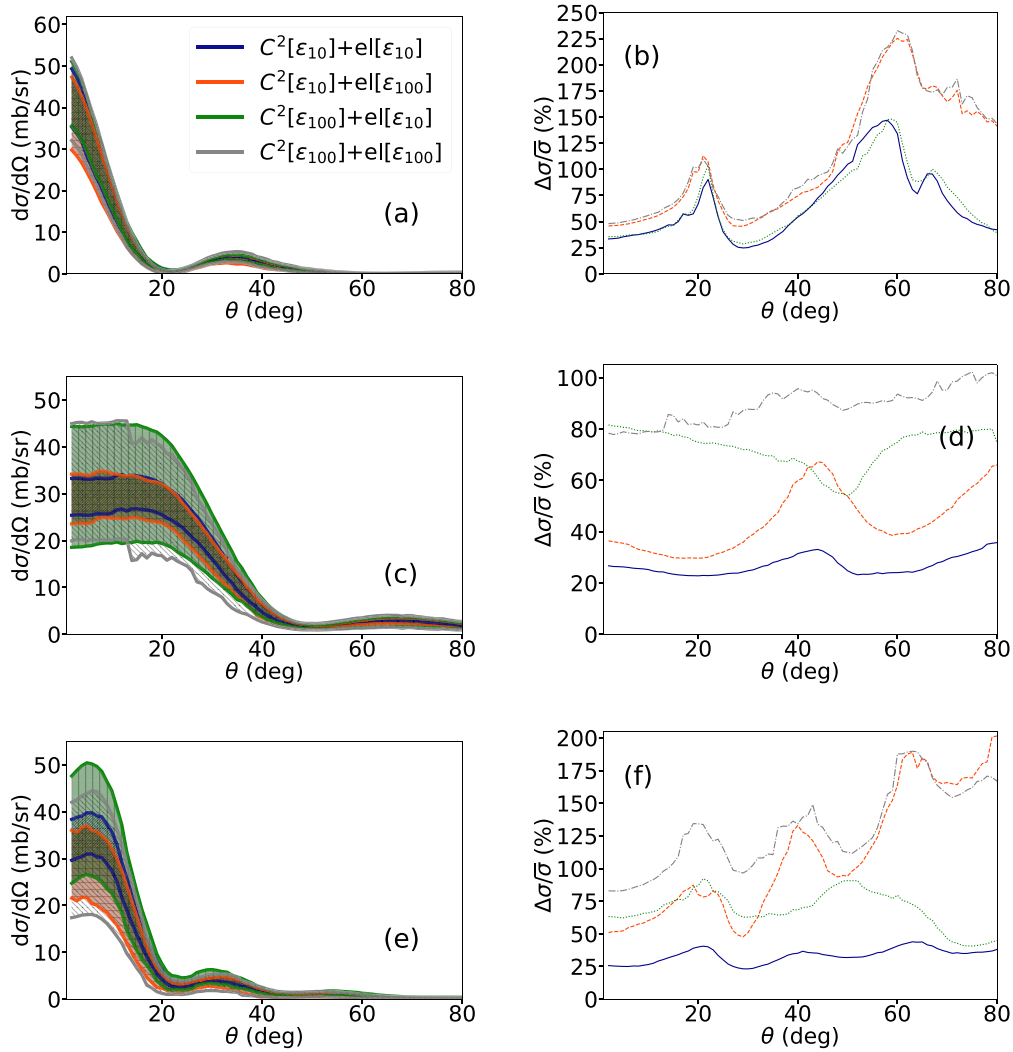

FIG. 4. A comparison of results using different combinations of ANC (C^2) and elastic (el) constrains, 10% error on both the ANC and the elastic data in blue, 10% error on the ANC and 100% error on the elastic in red, 10% error on the elastic and 100% error on the ANC in green, and unconstrained ANC and elastic data (100% error on both) in gray. (a) and (b) ^{14}C(d,p) at 17-MeV 68% confidence intervals and percentage uncertainty plot. (c) and (d) ^{16}O(d,p) at 15-MeV 68% confidence intervals and percentage uncertainty plot. (e) and (f) ^{48}Ca(d,p) at 24 MeV 68% confidence intervals and percentage uncertainty plot.

V. CONCLUSIONS

In this study we present the first complete quantification of parametric uncertainties in (d,p) transfer cross sections. We extend previous work focused on the quantification of uncertainties from the optical potentials to include the uncertainties associated with the final bound state. While the optical potential parameters are constrained through elastic-scattering mock data, the bound state is constrained with the asymptotic normalization coefficient extracted from an independent measurement. This choice is based on previous work that indicated the usefulness of the ANC in reducing the ambiguity of the bound-state overlap function.

As in previous studies, we use a Bayesian MCMC framework to determine parameter posterior distributions, and we propagate these to the transfer cross sections, generating the 68% and 95% confidence intervals for the angular distributions. We consider three reactions: ^{14}C$(d,p)^{15}$C(g.s.) at $E_d = 17$ MeV; ^{16}O$(d,p)^{17}$O(g.s.) at $E_d = 15$ MeV; and ^{48}Ca$(d,p)^{49}$Ca(g.s.) at $E_d = 24$ MeV. These reactions include a wide range of separation energies and angular momentum of the final state. Of the three, the reaction on ^{14}C is unique because it populates an s-wave halo state that is loosely bound.

We compare results using a standard 10% error on the data (an error achievable for many current experiments) versus a 100% error on the data, the latter representing minimal information from experiment. Our results demonstrate conclusively that introducing the additional constraint on the bound-state parameters through the ANC, on top of the constraints on the optical potential parameters through the elastic-scattering data, reduces the uncertainty on the transfer cross section. This reduction is more noticeable for the reactions more sensitive to the interior, because it is for those reactions that the ambiguities associated with the bound-state mean field are the largest.

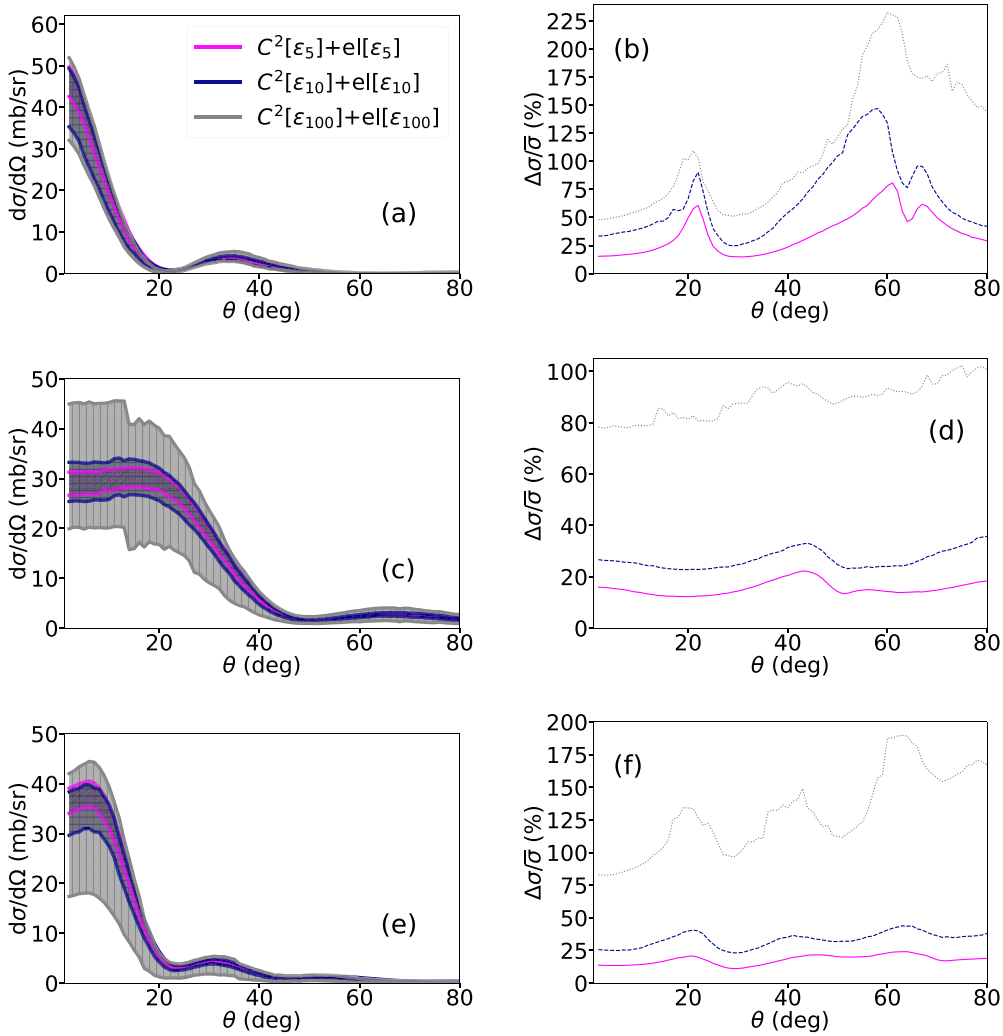

FIG. 5. A comparison of results using different errors on both ANC (C^2) and elastic (el) data, 5% error in magenta, 10% error in blue, and unconstrained data (100% error) in gray. (a) and (b) ^{14}C(d,p) at 17-MeV 68% confidence intervals and percentage uncertainty plot. (c) and (d) ^{16}O(d,p) at 15-MeV 68% confidence intervals and percentage uncertainty plot; (e) and (f) ^{48}Ca(d,p) at 24-MeV 68% confidence intervals and percentage uncertainty plot.

It is important to note that for peripheral reactions (such as the reaction on ^{14}C studied here), the cross section is approximately proportional to the ANC squared and, therefore, the cross section should be parametrized directly in terms of the ANC. What we quantify in this work is the uncertainty from the mean field. Our results show that the ANC is not as stringent a constraint on the single-particle parameters of the bound state as for the nonperipheral reactions.

We also show how misleading the uncertainty quantification can be when one ignores the uncertainties associated with a set of interactions. Keeping the interactions fixed (assuming zero error) leads to erroneously small uncertainties that do not correspond to reality. The low limit for the percent width of the 68% confidence interval on the transfer cross section when minimal information is available on both optical potentials and bound-state interactions close to ≈100%. This number is greatly reduced by introducing constraints on the optical potential and the bound-state interaction: ≈30%.

Finally, we consider the prospect of having high-precision experiments with 5% error, given the continual advances in accelerator and detector technologies. For such cases, the percent 1σ width of the transfer-cross-section angular distribution stays consistently around 15% for all reactions considered, a factor of 2 lower than that obtained when the experimental data have a 10% error.

This work relies on a specific reaction model, namely, the ADWA. Although it accounts for deuteron breakup, it simplifies the deuteron three-body wave function by making the adiabatic approximation. In addition, this study assumes only pairwise interactions. These simplifications may introduce model uncertainties that are not yet quantified. More work is needed to address model uncertainties. Given the computational cost of exact three-body calculations, a necessary step to proceed with the quantification of model uncertainties is the development of fast and reliable emulators, along the lines of what was done in Ref. [38].

ACKNOWLEDGMENTS

This work was supported by the U.S. Department of Energy under Grant No. DE-SC0021422. This work was performed under the auspices of the U.S. Department of Energy by Los Alamos National Laboratory under Contract No. 89233218CNA000001. A.E.L. acknowledges the support of the Laboratory Directed Research and Development program of Los Alamos National Laboratory. This work relied on iCER and the High Performance Computing Center at Michigan State University for computational resources.

[1] D. W. Bardayan, J. Phys. G: Nucl. Part. Phys. **43**, 043001 (2016).
[2] K. Wimmer, J. Phys. G: Nucl. Part. Phys. **45**, 033002 (2018).
[3] A. H. Wuosmaa, B. B. Back, S. Baker, B. A. Brown, C. M. Deibel, P. Fallon, C. R. Hoffman, B. P. Kay, H. Y. Lee, J. C. Lighthall *et al.*, Phys. Rev. Lett. **105**, 132501 (2010).
[4] D. Walter, S. D. Pain, J. A. Cizewski, F. M. Nunes, S. Ahn, T. Baugher, D. W. Bardayan, T. Baumann, D. Bazin, S. Burcher *et al.*, Phys. Rev. C **99**, 054625 (2019).
[5] S. V. Szwec, D. K. Sharp, B. P. Kay, S. J. Freeman, J. P. Schiffer, P. Adsley, C. Binnersley, N. de Séréville, T. Faestermann, R. F. Garcia Ruiz *et al.*, Phys. Rev. C **104**, 054308 (2021).
[6] B. P. Kay, J. P. Schiffer, S. J. Freeman, T. L. Tang, B. D. Cropper, T. Faestermann, R. Hertenberger, J. M. Keatings, P. T. MacGregor, J. F. Smith *et al.*, Phys. Rev. C **103**, 024319 (2021).
[7] I. J. Thompson and F. M. Nunes, *Nuclear Reactions for Astrophysics* (Cambridge University, Cambridge, England, 2009).
[8] R. Johnson and P. Tandy, Nucl. Phys. A **235**, 56 (1974).
[9] C. Hebborn, F. M. Nunes, G. Potel, W. H. Dickhoff, J. W. Holt, M. C. Atkinson, R. B. Baker, C. Barbieri, G. Blanchon, M. Burrows *et al.*, J. Phys. G: Nucl. Part. Phys. **50**, 060501 (2023).
[10] A. E. Lovell and F. M. Nunes, J. Phys. G: Nucl. Part. Phys. **42**, 034014 (2015).
[11] A. E. Lovell, F. M. Nunes, J. Sarich, and S. M. Wild, Phys. Rev. C **95**, 024611 (2017).
[12] A. E. Lovell and F. M. Nunes, Phys. Rev. C **97**, 064612 (2018).
[13] G. B. King, A. E. Lovell, and F. M. Nunes, Phys. Rev. C **98**, 044623 (2018).
[14] G. B. King, A. E. Lovell, L. Neufcourt, and F. M. Nunes, Phys. Rev. Lett. **122**, 232502 (2019).
[15] M. Catacora-Rios, G. B. King, A. E. Lovell, and F. M. Nunes, Phys. Rev. C **100**, 064615 (2019).
[16] A. E. Lovell, F. M. Nunes, M. Catacora-Rios, and G. B. King, J. Phys. G: Nucl. Part. Phys. **48**, 014001 (2020).
[17] M. Catacora-Rios, G. B. King, A. E. Lovell, and F. M. Nunes, Phys. Rev. C **104**, 064611 (2021).
[18] A. M. Mukhamedzhanov and F. M. Nunes, Phys. Rev. C **72**, 017602 (2005).
[19] A. M. Mukhamedzhanov, F. M. Nunes, and P. Mohr, Phys. Rev. C **77**, 051601(R) (2008).
[20] N. C. Summers and F. M. Nunes, Phys. Rev. C **78**, 011601(R) (2008).
[21] A. M. Mukhamedzhanov, V. Burjan, M. Gulino, Z. Hons, V. Kroha, M. McCleskey, J. Mrázek, N. Nguyen, F. M. Nunes, Š. Piskoř *et al.*, Phys. Rev. C **84**, 024616 (2011).
[22] J. M. Mueller, R. J. Charity, R. Shane, L. G. Sobotka, S. J. Waldecker, W. H. Dickhoff, A. S. Crowell, J. H. Esterline, B. Fallin, C. R. Howell *et al.*, Phys. Rev. C **83**, 064605 (2011).
[23] A. Tellez, R. Ballini, J. Delaunay, and J. Fouan, Nucl. Phys. A **127**, 438 (1969).
[24] R. H. McCamis, T. N. Nasr, J. Birchall, N. E. Davison, W. T. H. van Oers, P. J. T. Verheijen, R. F. Carlson, A. J. Cox, B. C. Clark, E. D. Cooper *et al.*, Phys. Rev. C **33**, 1624 (1986).
[25] G. Schreder, W. Grum, J. W. Hammer, K.-W. Hoffmann, and G. Schleussner, Phys. Rev. C **39**, 1774 (1989).
[26] S. Kobayashi, J. Phys. Soc. Jpn. **15**, 1164 (1960).
[27] T. Curtis, H. Lutz, D. Heikkinen, and W. Bartolini, Nucl. Phys. A **165**, 19 (1971).
[28] G. Murillo, M. Fernández, J. Ramirez, M. Mejia-Gil, R. Policroniades, A. Varela, S. Darden, S. Sen, R. Prior, and E. Chavez, Rev. Mex. Fis. S **57**, 55 (2011).
[29] D. R. Phillips, R. J. Furnstahl, U. Heinz, T. Maiti, W. Nazarewicz, F. M. Nunes, M. Plumlee, M. T. Pratola, S. Pratt, F. G. Viens *et al.*, J. Phys. G: Nucl. Part. Phys. **48**, 072001 (2021).
[30] L. J. Titus, F. M. Nunes, and G. Potel, Phys. Rev. C **93**, 014604 (2016).
[31] A. Koning and J. Delaroche, Nucl. Phys. A **713**, 231 (2003).
[32] J. D. Goss, P. L. Jolivette, C. P. Browne, S. E. Darden, H. R. Weller, and R. A. Blue, Phys. Rev. C **12**, 1730 (1975).
[33] E. L. Keller, Phys. Rev. **121**, 820 (1961).
[34] F. D. Becchetti, Jr. and G. Greenlees, Phys. Rev. **182**, 1190 (1969).
[35] I. J. Thompson, Comput. Phys. Rep. **7**, 167 (1988).
[36] L. Titus, A. Ross, and F. Nunes, Comput. Phys. Commun. **207**, 499 (2016).
[37] J.-M. Sparenberg, P. Capel, and D. Baye, Phys. Rev. C **81**, 011601(R) (2010).
[38] O. Sürer, F. M. Nunes, M. Plumlee, and S. M. Wild, Phys. Rev. C **106**, 024607 (2022).